DTU Library

Experimental characterization of a shape optimized acoustic lens: Application to compact speakerphone design

Andersen, Peter Risby; Lee, Gyeong-Tae; Nielsen, Daniel Gert; Kook, Junghwan; Cutanda Henríquez, Vicente; Aage, Niels; Park, Yong-Hwa

Published in:
Journal of the Acoustical Society of America

Link to article, DOI:
10.1121/10.0017859

Publication date:
2023

Document Version
Publisher's PDF, also known as Version of record

APRIL 19 2023

Experimental characterization of a shape optimized acoustic lens: Application to compact speakerphone design

Peter Risby Andersen; Gyeong-Tae Lee; Daniel Gert Nielsen; ... et. al

J Acoust Soc Am 153, 2351 (2023)
https://doi.org/10.1121/10.0017859

JASA ARTICLE

Experimental characterization of a shape optimized acoustic lens: Application to compact speakerphone design

Peter Risby Andersen,[1] Gyeong-Tae Lee,[2] Daniel Gert Nielsen,[1] Junghwan Kook,[1,a)]
Vicente Cutanda Henríquez,[3] Niels Aage,[4] and Yong-Hwa Park[2]

[1]*GN Audio A/S & Jabra, Audio Research, Lautrupbjerg 7, 2750 Ballerup, Denmark*

[2]*Department of Mechanical Engineering, Korea Advanced Institute of Science and Technology, Daejeon 34141, South Korea*

[3]*Centre for Acoustic-Mechanical Micro Systems, Department of Electrical and Photonics Engineering, Technical University of Denmark, Ørsteds Plads, Building 352, DK-2800, Kgs. Lyngby, Denmark*

[4]*Centre for Acoustic-Mechanical Micro Systems, Department of Civil and Mechanical Engineering, Technical University of Denmark, Koppels Allé, Building 404, DK-2800, Kgs. Lyngby, Denmark*

ABSTRACT:
This work presents the shape optimization and subsequent experimental validation of an acoustic lens with application to a compact loudspeaker, such as found in commercial speakerphones. The shape optimization framework is based on a combined lumped parameter and boundary element method model using free form deformation geometry parameterization. To test the optimized design, the loudspeaker lens is three-dimensionally printed and experimentally characterized under anechoic conditions on a finite baffle with respect to its off-axis frequency response. The overall tendencies of the frequency responses agree well between measurement and simulations within the optimization frequency range and at low frequencies. The optimization process is applied to a model including acoustic lumped parameter approximations. The shortcomings of the assumptions made in the model are revealed by laser Doppler vibrometer measurements of the loudspeaker driver and modelling of the mechanical vibrations of the lens. https://doi.org/10.1121/10.0017859

(Received 13 December 2022; revised 10 March 2023; accepted 30 March 2023; published online 19 April 2023)

[Editor: Mingsian R. Bai] Pages: 2351–2361

I. INTRODUCTION

Speakerphones are compact communication devices typically used for online conferencing calls. They consist of a loudspeaker system designed to radiate speech from an online meeting to multiple participants in a meeting room. Speakerphones also have several built-in microphones that are used to pick up speech signals from the meeting participants. Many speakerphones are designed as lightweight portable devices that can be placed on a table in a meeting room. In a typical meeting, scenario participants are located around a table; hence, it is important that the acoustic energy of the speaker is directed toward the listening positions of the meeting participants.

Acoustic lenses can be used to control the directivity of a loudspeaker system. As an example, Mellow and Kärkkäinen recently showed how the scattering of a disk source by a rigid sphere can be modelled analytically and used their result to broaden the directivity of a loudspeaker-like structure (Mellow and Kärkkäinen, 2022). A wide range of high-end loudspeaker products also utilize acoustic lens concepts to control the radiation pattern, e.g., the Bang and Olufsen Beolab 20 (Struer, Denmark) (Bang and Olufsen, 2014). The design of acoustic lenses is also an active field of research within the area of acoustic metamaterials (Dong *et al.*, 2017; Gao *et al.*, 2019) and topology optimization (Christiansen and Sigmund, 2016).

Shape optimization is a valuable engineering tool for improving the design of acoustic devices and can potentially be used to change the radiation properties of loudspeaker systems, such as the speakerphone. Considering acoustics, shape optimization has been applied in multiple areas including the design of noise reducing partitions (Van den Wyngaert *et al.*, 2021) and acoustic scattering of submarines (Chen *et al.*, 2019), to name a few. More relevant to the scope of this work, much of the existing literature on acoustic shape optimization has treated the design of acoustic horns. Based on an axisymmetric boundary element method (BEM), Udawalpola *et al.* improve the radiation efficiency of an acoustic horn using gradient-based shape optimization (Udawalpola *et al.*, 2011). The same authors have also treated optimization of the far-field radiation from horns using the finite element method (FEM) (Udawalpola and Berggren, 2008). Similarly, Bängtsson *et al.* perform two-dimensional (2D) FEM-based shape optimization minimizing the reflection coefficient of an acoustic horn (Bängtsson *et al.*, 2003). The above examples of horn optimization are conducted using a frequency domain representation of the acoustic problems which can make wideband optimization difficult. In a more recent publication, Schmidt *et al.* use a three-dimensional (3D) discontinuous Galerkin FEM time-domain modelling

[a)]Electronic mail: jkook@jabra.com

approach to perform wideband large-scale horn optimization (Schmidt *et al.*, 2016).

Different optimization strategies have also been applied to optimize transducers such as a loudspeaker driver. Bezzola presents shape and topology optimization strategies for loudspeaker design (Bezzola, 2018). Similarly, Christensen has several examples of how optimization can be used to optimize the shape of a loudspeaker cone, magnet, basket, and heat sink (Christensen, 2020). Moreover, Nielsen *et al.* have shown how distributed vibroacoustic material optimization of the diaphragm and the surround of the loudspeaker can result in an extended flat and wideband behaviour (Nielsen *et al.*, 2021). Vibroacoustic examples of hearing instrument optimization also exist. Creixell Mediante *et al.* use a reduced order model to perform parameter optimization of a hearing instrument (Creixell Mediante *et al.*, 2018). In a very recent publication, Dilgen *et al.* show how vibroacoustic FEM cut-element–based topology optimization can be used to optimize a full-sized hearing instrument (Dilgen *et al.*, 2022).

This work presents experimental characterization of a loudspeaker system with an acoustic lens designed by numerical shape optimization. The underlying numerical model is based on the BEM for exterior acoustic field calculations and a lumped parameter model (LPM) of the loudspeaker. The optimization procedure is based on a classical free form deformation (FFD) approach utilizing trivariate Bernstein polynomials for the mesh parameterization (Sederberg, 1986). Moreover, to correct for high-frequency inaccuracies in the LPM, additional radially distributed laser Doppler vibrometer (LDV) velocity measurements are conducted and used as boundary conditions in the BEM to verify measurement results. The optimized loudspeaker is tested in terms of sound pressure level (frequency responses) at different angles in front of the loudspeaker. The experimental work shows the feasibility of the acoustic shape optimization framework for acoustic loudspeaker design, but also its limitations with respect to the accuracy of the underlying loudspeaker modelling. It should be noted that the work is a natural continuation of the work recently published in Andersen *et al.* (2022a).

The paper is organized as follows: First, the computational modelling and optimization approach is presented. This is followed by sections describing the optimization results, 3D printing of the design, and measurement. Finally, the findings are discussed and conclusions are drawn.

II. NUMERICAL MODEL OF ONE-EIGHTH LOUDSPEAKER ON AN INFINITE BAFFLE

This section introduces the geometry of the loudspeaker that is to be optimized and the underlying numerical model. A rendering of the entire geometry of the up-firing loudspeaker is depicted in Fig. 1. To reduce the computational complexity, the geometry is modelled using one-eighth mirrored symmetry. Applying one-eighth mirrored symmetry puts some limitations on what vibrations of the loudspeaker can be modelled, i.e., asymmetrical breakup modes of the loudspeaker cannot be included. The computational mesh of the one-eighth up-firing loudspeaker and the sizing parameters are shown in Fig. 2. The computational model contains a boundary Γ_a, describing the geometry of the loudspeaker cabinet and the acoustic lens (shown in blue color in Fig. 2). The exterior geometry of the loudspeaker driver is given by the boundary Γ_b. During the optimization, the lens geometry is considered as detached from the cabinet. Support structures will first be added as part of the fabrication and measurement process of the loudspeaker system. This has been justified by preliminary simulations that have shown that the effect of the support structures is minimal within the frequency range of optimization.

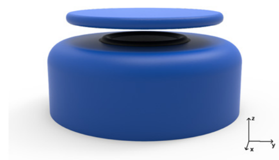

FIG. 1. (Color online) Rendering of the entire initial geometry of the loudspeaker system.

A. Boundary element method

The exterior acoustic field is modelled using BEM with one-eighth symmetry around the z-axis and an infinite baffle at $z = 0$. The starting point for the BEM is the Kirchhoff–Helmholtz surface integral equation given by

$$C(P_j)p(P_j) = \int_\Gamma \frac{\partial G_s}{\partial n} p(Q) \mathrm{d}\Gamma(Q) - \int_\Gamma G_s \frac{\partial p(Q)}{\partial n} \mathrm{d}\Gamma(Q), \quad (1)$$

where P_j is a collocation point, Q is an integration point on the generator, Γ is the boundary, p is the acoustic pressure, and G_s is the Green's function containing contributions from symmetry conditions. Hence, due to the one-eighth symmetry and the infinite baffle condition, the Green's function is expressed as

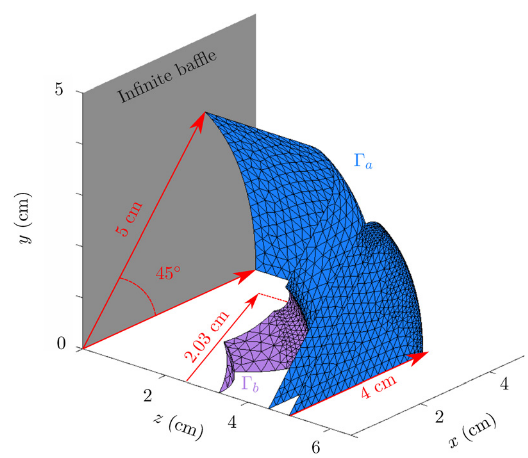

FIG. 2. (Color online) The computational mesh used for boundary element simulations utilizing one-eighth symmetry and the corresponding dimensions. The complete computational boundary (Γ) consists of the cabinet and the lens (Γ_a), and the loudspeaker (Γ_b).

$$G_s = \sum_{j}^{N_p} \frac{e^{-ikR}}{R}, \tag{2}$$

with $R = |P_j - Q|$ being the distance between a collocation point and an integration point. For a problem with eights symmetry and an infinite baffle $N_p = 16$. Here, velocity boundary excitation is only applied in the z-direction (piston motion of the diaphragm and only excitation on Γ_b). Therefore, the Kirchhoff–Helmholtz integral is rewritten as

$$C(P_j)p(P_j) = \int_\Gamma \frac{\partial G_s}{\partial n} p(Q)\mathrm{d}\Gamma(Q) + i\omega\rho\int_{\Gamma_b} G_s n_z u_z \mathrm{d}\Gamma(Q), \tag{3}$$

using Euler's equation. In Eq. (3), ω is the angular frequency, ρ is the density of air, n_z is the z-component of the surface normal vector, and u_z is the velocity in the z-direction. Here, the geometry is discretized with quadratic isoparametric elements and the final mesh consists of 6255 nodes and 3033 elements. This corresponds to an element size of approximately 2.1 mm which equates to more than 29 elements per wavelength at the highest optimization frequency. After the discretization of Eq. (3), the BEM system of equations becomes

$$\mathbf{A}\mathbf{p} + i\omega\rho\mathbf{B}_{\Gamma_b}\mathbf{u}_{z,\Gamma_b} = \mathbf{0}, \tag{4}$$

where $\mathbf{A}$ and $\mathbf{B}_{\Gamma_b}$ are the matrices created from the discretization of the double and single layer potentials, respectively. It is noted that the single layer potential is only evaluated at Γ_b since $u_z = 0$ on Γ_a is assumed. Moreover, $\mathbf{p}$ is a vector with the acoustic complex pressures and $\mathbf{u}_z$ is a vector with the complex surface velocities in the z-direction. The BEM implementation is based on a mixed MATLAB (Natick, MA) and C++/MEX environment parallized with OpenMP, with the assembly routine being inspired by the OpenBEM MATLAB BEM implementation (Juhl and Cutanda Henríquez, 2010).

B. Lumped parameter coupling

The first method that is used to model the behaviour of the loudspeaker is a LPM coupling to the BEM. Combining lumped parameter modelling and numerical models with meshes, such as the FEM and the BEM, is advantageous as it reduces the model complexity (Bai *et al.*, 2009; Nielsen *et al.*, 2020). A more elaborate explanation of the coupling approach and the description of the individual lumped elements can be found in Andersen *et al.* (2022a). From the reference, the coupled system of equations becomes

$$\begin{bmatrix} \mathbf{A} & i\omega\rho\mathbf{B}_{\Gamma_b} & \mathbf{0} & \mathbf{0} \\ \mathbf{0} & \mathbf{C}_p & \mathbf{0} & -\mathbf{c}_{\Gamma_b} \\ \mathbf{0} & \mathbf{0} & Z_E & Bl \\ \zeta\mathbf{s}_n & \mathbf{0} & -Bl & (Z_{MD} + S_D^2 Z_{AB}) \end{bmatrix} \begin{bmatrix} \mathbf{p} \\ \mathbf{u}_{z,\Gamma_b} \\ i_c \\ u_D \end{bmatrix} = \begin{bmatrix} \mathbf{0} \\ \mathbf{0} \\ V_0 \\ 0 \end{bmatrix}, \tag{5}$$

where $\mathbf{C}_p$ is a coupling matrix, $\mathbf{c}_{\Gamma_b}$ is a coupling vector, Z_E is the electrical impedance, Bl is the force factor, $\mathbf{s}_n$ is the pressure coupling vector, $\zeta = 8$ arises due to symmetry, Z_{MD} is the mechanical impedance, S_D is the equivalent surface area of the diaphragm, Z_{AB} is the acoustic impedance of the interior of the cabinet, i_c is the electrical current, V_0 is the driving voltage, and u_D is the lumped velocity of the diaphragm. A more elaborate introduction to the definition of the LPM parameters can be found in Leach (2010). The electrical, mechanical, and the acoustic impedances are found as

$$Z_E = R_E + L_E(\omega), \tag{6}$$

$$Z_{MD} = i\omega M_{MD} + R_{MS} + (i\omega C_{MS})^{-1}, \tag{7}$$

$$Z_{AB} = i\omega M_{AB} + R_{AB} + (i\omega C_{AB})^{-1}, \tag{8}$$

where R_e is the DC resistance of the voice-coil, $L_E(\omega)$ is the frequency dependent inductance of the voice-coil, M_{MD} is mass of the diaphragm and voice-coil, R_{MS} is the mechanical losses, C_{MS} is the compliance of the mechanical suspension, M_{AB} is the acoustic mass of the enclosure, R_{AB} is the acoustic resistance due to filling material, and C_{AB} is the compliance of the enclosure. The LPM parameters used in the optimization are given in Table I. The matrix equation in Eq. (5) is solved using the generalized minimal residual method (GMRES).

III. PARAMETERIZATION

The boundary element mesh is parameterized using FFD relying on Bernstein polynomials in a cylindrical coordinate system. Assuming cylindrical coordinates, the mesh is mapped to a parameter space that is given by

$$\begin{bmatrix} r(s) \\ \theta(t) \\ z(u) \end{bmatrix} = \sum_{i=0}^{l}\sum_{j=0}^{m}\sum_{k=0}^{n} B_{i,l}(s)B_{j,m}(t)B_{k,n}(u) \begin{bmatrix} r_{i,j,k} \\ \theta_{i,j,k} \\ z_{i,j,k} \end{bmatrix}, \tag{9}$$

where $0 < s < 1$, $0 < t < 1$, and $0 < u < 1$ are the local parameters that form the FFD region. The control points that

TABLE I. Lumped parameter elements used during the optimization.

Electrical lumped elements			
V_0 (V)	R_E (Ω)	L_1 (H)	Bl (T m)
$\sqrt{2}$	2.61	$8.5 \cdot 10^{-5}$	2.558
L_2 (H)	R_2 (Ω)	$L_E(\omega)$ (H)	
$8.1 \cdot 10^{-5}$	0.67	$i\omega L_1 + \dfrac{\omega^2 L_2 R_2 + i\omega L_2 R_2^2}{\omega^2 L_2^2 + R_2^2}$	
Mechanical lumped elements			
M_{MD} (kg)	R_{MS} (N s m^{-1})	C_{MS} (m N^{-1})	S_D (m^2)
$1.8 \cdot 10^{-3}$	0.287	$9.25 \cdot 10^{-4}$	$1.3 \cdot 10^{-3}$
Acoustical lumped elements			
C_{AB} (m^5 N^{-1})	R_{AB} (N s m^{-5})	M_{AB} (kg m^4)	
$1.62 \cdot 10^{-9}$	200	626	

https://doi.org/10.1121/10.0017859

can be used to distort the geometry are given by the $r_{i,j,k}$, $\theta_{i,j,k}$, and $z_{i,j,k}$ coordinates. Moreover, in the FFD region, the number and the distribution of the control points can be controlled from the integers l, m, and n. Also, it is chosen to use Bernstein basis functions given by

$$B_{i,l}(s) = \binom{l}{i} s^i (1-s)^{l-i}, \tag{10}$$

with $B_{j,m}$ and $B_{k,n}$ being defined in the same way. Bernstein polynomials are chosen as they have the benefit of ensuring a degree of mesh regularization as compared to more local interpolation methods with compact support. Mapping of the Cartesian coordinates in the boundary element mesh onto the FFD region can be found by the transformation

$$x(s,t) = r(s)\cos(\theta(t)), \tag{11}$$

$$y(s,t) = r(s)\sin(\theta(t)), \tag{12}$$

$$z(u) = z(u). \tag{13}$$

For the optimization example presented here, two FFD regions are created: one covering the deformation of the lens and a second region changing the shape of the loudspeaker cabinet. The two FFD regions and the associated control points are shown in Fig. 3. The size and location of a FFD region is given by the smallest and largest cylindrical coordinate of the control points, hereafter, denoted with the subscripts *min* and *max*, respectively. For the FFD region controlling the shape of the lens (Region 1 in Fig. 3), the following values are used: $l = 6$, $m = 6$, $n = 1$, $r_{min} = 0$ cm, $r_{max} = 4.1$ cm, $\theta_{\min} = 0°$, $\theta_{\max} = 45°$, $z_{min} = 4.3$ cm, and $z_{max} = 5.2$ cm. The second FFD region controlling the cabinet shape (Region 2 in Fig. 3) is given by: $l = 6$, $m = 8$, $n = 1$, $r_{min} = 2.8$ cm, $r_{max} = 5.1$ cm, $\theta_{\min} = 0°$, $\theta_{\max} = 45°$, $z_{min} = 1$ cm, and $z_{max} = 3.8$ cm.

Notice for the here presented optimization problem control points are only allowed to move in the z-direction. This is conducted to reduce the number of design variables used

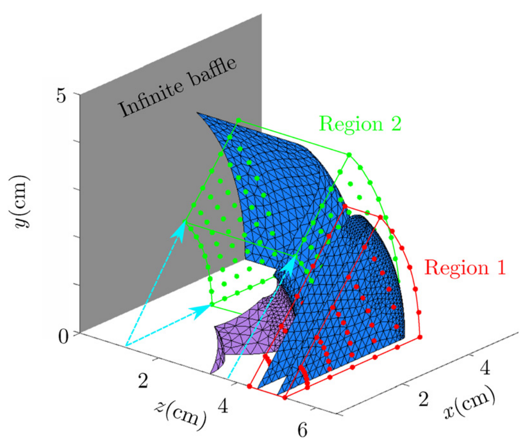

FIG. 3. (Color online) The two FFD regions used to control the shape of the lens (Region 1) and the LS cabinet (Region 2). The green and red dots represent the location of the control points. Also, the cyan dashed arrows indicate the location of Region 2 with respect to the z-axis.

in the optimization and lower the optimization time. Therefore, the optimization will have less design freedom. Also, in the FFD region covering the lens, the control points with the same θ- and r-coordinates are linked together to form a single design variable. A more elaborate description of the linking approach can be found in Andersen *et al.* (2022a). In general, this is conducted to avoid collision of the two opposite surfaces of the lens and create nonphysical designs. For the FFD region covering the cabinet, only control points at $z = 3.8$ cm are allowed to move, i.e., control points close to the top of the cabinet. This simplifies the optimization problem by reducing the number of design variables. However, it also restricts the design space. Consequently, one might lose some performance from the optimization. Nonetheless, it ensures that the mesh quality remains sufficient during the optimization.

IV. OPTIMIZATION PROBLEM

The objective of the optimization is to improve the flatness of the frequency response and the off-axis distribution of the sound pressure level (SPL). One possible way to formulate this in terms of a cost function is to minimize the least square difference between the SPL and a target value at different optimization frequencies. A similar cost function description has been used by Nielsen *et al.* for loudspeaker optimization (Nielsen *et al.*, 2021). Hence, the objective function is given by

$$\phi_k(\mathbf{v}, T) = \sum_{i}^{N_i} \sum_{j}^{N_j} |T - SPL(r_d, \theta_i, \psi_j, \mathbf{v})|^2, \tag{14}$$

where $\phi_k(\mathbf{v}, T)$ is the cost function at the k-th frequency as a function of the control points location represented by the vector $\mathbf{v}$ and the target value T. The target value T is a scalar that is constant with frequency, but its value is given as a design variable during the optimization. This provides some flexibility for the optimizer to adjust the output SPL. However, it might be undesirable if a maximum of the output in the optimization region is sought. Nevertheless, this is performed as it relaxes the optimization difficulty, and we therefore accept some decrease in output SPL. The SPL is evaluated at discrete field points given by $SPL(r_d, \theta_i, \psi_j, \mathbf{v})$, where r_d, θ_i and ψ_j are the distance from the origin to the field point, the azimuth angle, and the elevation angle, respectively. For time harmonic oscillations, the SPL is given by Kinsler (2000),

$$\mathrm{SPL}(r_d, \theta_i, \psi_j, \mathbf{v}) = 20\log_{10}\left(\frac{\frac{1}{\sqrt{2}}|p(r_d, \theta_i, \psi_j, \mathbf{v})|}{p_{ref}}\right), \tag{15}$$

where $p_{ref} = 20\ \mu$Pa. The distribution of the field points used during the optimization is depicted in Fig. 4. The field points are distributed using the following parameters: $r_d = 30$ cm, $0° \leq \theta_i \leq 45°$ with $N_i = 18$, and $35° \leq \psi_j \leq 75°$ with $N_j = 12$. As is observed, this example covers a wide range of angles defined by ψ_j. This distribution will depend

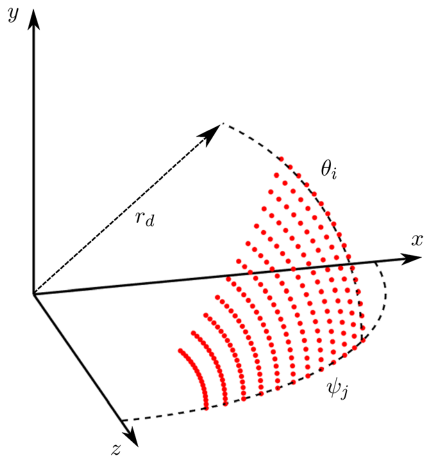

FIG. 4. (Color online) A sketch of the field points where $SPL(r_d, \theta_i, \psi_j)$ is evaluated.

on the speakerphone use case, i.e., the size of the table and the distance to the meeting participants, etc. Using a wide range of optimization angles will potentially make the device more robust to different use cases. Nevertheless, it will also make the optimization problem more difficult.

A multi-frequency optimization problem can be stated in many different methods. To achieve a flat response in the entire optimization range, it is possible to formulate the problem as a *minimax* problem (Andersen *et al.*, 2022a; Nielsen *et al.*, 2021). When using a minimax formulation, the cost function at the worst performing frequency is minimized. Formally, this can be written as

$$\begin{aligned} \min_{\mathbf{v},T} \quad & \max_k \phi_k(\mathbf{v}, T) \\ \text{s.t.} \quad & \text{Eq. (5)} \\ & 0 \le v_l \le 1, \\ & 70 \le T \le 90, \end{aligned} \tag{16}$$

where v_l is a single entry in $\mathbf{v}$. The z-location of the control points, i.e., the design variables, are scaled from zero to one using

$$v_l = \frac{z_{i,j,k} - L_l}{L_u - L_l}, \tag{17}$$

where L_u and L_l are the upper and lower bounds of the box constraints on the design variables. For the FFD Region 1 (see Fig. 3), $L_u = 7.2$ cm and $L_l = 4.9$ cm. The limits of Region 2 (also see Fig. 3) are $L_u = 4$ cm and $L_l = 1.56$ cm. The optimization problem in Eq. (16) is solved using the *fminimax* function in MATLAB, with the design gradients being calculated using a semi-analytical adjoint approach (Andersen *et al.*, 2022a).

V. OPTIMIZATION RESULT

The shape optimization is performed in the frequency range 1.5–5.5 kHz using a linear spacing of 250 Hz between optimization frequencies resulting in 17 optimization frequencies. Alternatively, a logarithmic spacing can be chosen as this can be considered more perceptually correct. Nevertheless, a linear spacing is chosen as this gives more weighting toward higher frequencies where the response is more sensitive to design changes. Moreover, the optimization is carried out at the DTU Computing Center (DCC) on a single node consisting of two Intel Xeon (Santa Clara, CA) E5–2650v4 computer processing units and 512 Gb of random access memory (DTU Computing Center, 2022). Overall, the entire computational time is more than 3 weeks, corresponding to approximately 12 096 core hours.

The evolution of ϕ_k at the individual optimization frequencies is plotted in Fig. 5. As might be observed from the optimization history, the optimization was stopped after 68 iterations. This was performed due to the large time constraints of running the optimization problem; hence, a local minimum of the optimization outcome is not guaranteed. Also, the cost function is far from zero at the last iteration. Nevertheless, it is the authors' experience that it is challenging to obtain near-zero cost function values for realistic acoustic multi-frequency optimization problems. This is due to the physical behaviour rather than numerical limitations.

The final optimized geometry of the lens and cabinet is shown in Figs. 6(a) and 6(b). Mainly, two design choices are observed: (i) the outer sides of the lens are lifted upwards and its center is close to the loudspeaker, (ii) small valleys are created in the cabinet. Furthermore, the SPL frequency responses of the initial and the optimized design are shown in Fig. 7. The response is plotted as the variation in the SPL at all the field points used in the optimization. In the figure, the green curve is the spread of the SPL over all field points for the initial design (Fig. 1), and the blue curve is the spread in the SPL of the optimized design [Fig. 6(a)]. Also, the red horizontal dashed and solid lines are the values of T for the initial and the optimized design, respectively. Analysing the result of the initial design, it is seen how adding the flat disk on top of the loudspeaker creates a peak close to 2.55 kHz which is followed by a notch at 3.6 kHz. The increase in the SPL is attributed to an acoustic

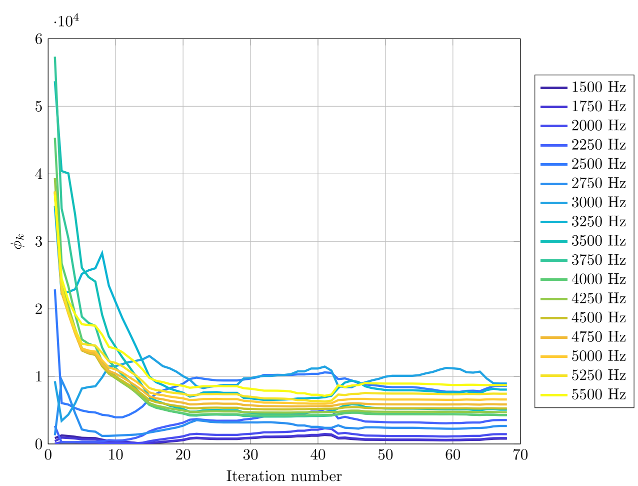

FIG. 5. (Color online) The evolution of ϕ_k at different optimization frequencies.

https://doi.org/10.1121/10.0017859

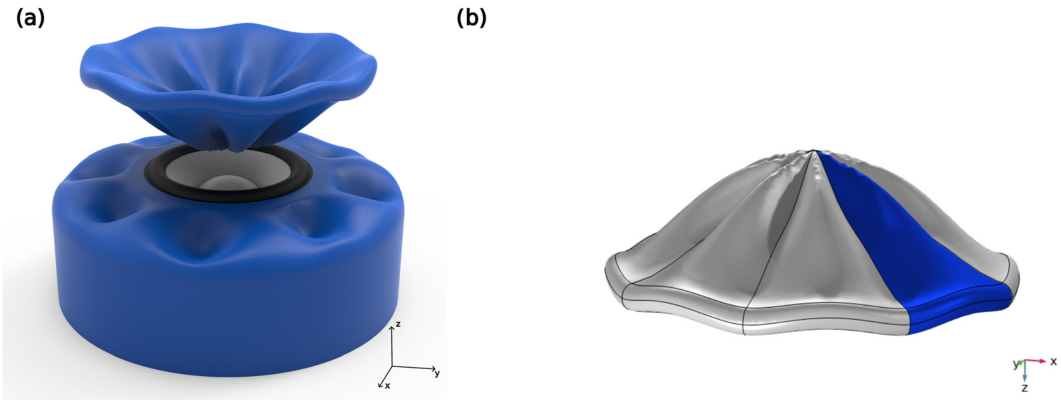

FIG. 6. (Color online) (a) Rendering of the optimized loudspeaker system, (b) view of the underside of the lens. The blue geometry highlights the one-eighth part that is used for the BEM simulations.

resonance arising between the loudspeaker and the lens. Similar behavior has also been observed in slit-firing speakers in, e.g., flat panel televisions (Lee *et al.*, 2015). On one hand, by comparing the initial and optimized design, it is evident that it is difficult to make significant changes to the response and its flatness. Nevertheless, the SPL response near the aforementioned acoustic resonance is flattened. The price paid is a larger variation in the SPL in this frequency region. On the other hand, the optimized geometry can increase the overall SPL magnitude between 3 and 6 kHz. Similar to the initial design, a very sharp notch is observed close to 3 kHz. This effect is an inherent property of the up-firing loudspeaker geometry and the outlet height between the loudspeaker box and the infinite baffle, which creates destructive interference between the source and its image behind the reflecting plane. As it is observed, it is possible to alter the frequency at which the sharp notch (cancellation) takes place. However, it is not possible to remove the effect.

VI. 3D PRINTING OF THE OPTIMIZED DESIGN

The acoustic lens and cabinet design is 3D printed using an HP Multi Jet Fusion (Palo Alto, CA) printer with the material PA-12 (also known as Nylon 12). To support the lens, a set of four cylindrical pillars is created that also works as mounting of the driver using four 3 mm bolts. The final 3D printed and assembled lens, cabinet, and driver are shown in Fig. 8.

VII. EXPERIMENTAL CHARACTERIZATION

The following section presents the results from the measurements of the loudspeaker system, which consists of the following two studies: First, a distributed velocity across the driver is measured. Second, the 3D printed optimized cabinet and lens is measured on top of a finite baffle to characterize its response at different angles.

A. Velocity boundary conditions from LDV measurements

A shortcoming of using the LPM model is the assumption of piston motion of the diaphragm. For higher frequencies, this assumption will become inaccurate due to breakup modes and a more complex vibration pattern. To improve the prediction of the loudspeaker behaviour at higher frequencies, a second simulation model is made where the velocity of the loudspeaker membrane is measured using an LDV.

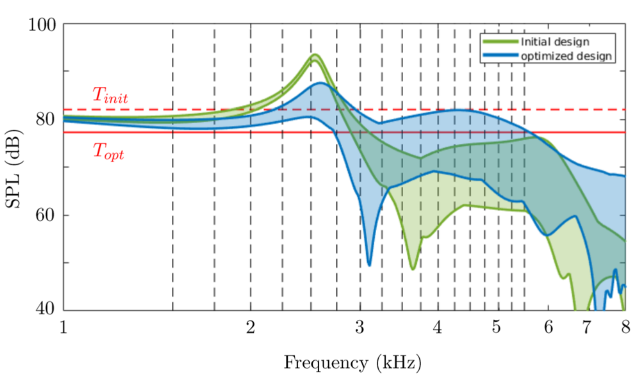

FIG. 7. (Color online) The frequency response of the initial (green curve) and optimized (blue curve) design. The curves represent the spread in the SPL among all the optimization field points, as seen in Fig. 4. The horizontal red dashed and solid lines represent the value to T for the initial and optimized response, respectively. Also, the vertical dashed lines are the locations of the discrete optimization frequencies.

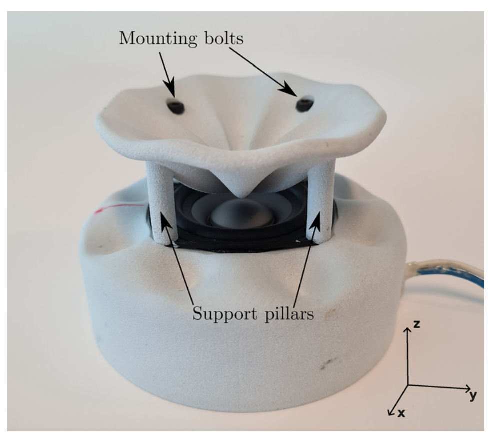

FIG. 8. (Color online) The 3D printed design including the loudspeaker driver.

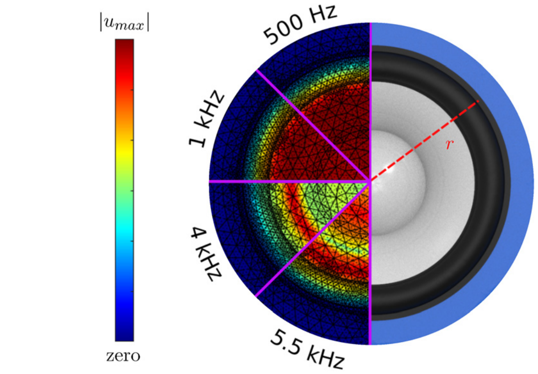

FIG. 9. (Color online) On the left-hand side, the distribution of the measured velocity amplitude at 500 Hz, and 1 4, and 5.5 kHz. The colormap is scaled from zero to the maximum amplitude for each frequency. The measured data used to create the colormap are based on the measured velocity amplitude and phase data in Figs. 10(a) and 10(b). On the right-hand side, the red dashed line is the definition of the radial line at which the velocity is measured with the LDV.

These measurements are performed by removing the lens. The measurement setup is very similar to what is presented in Collini *et al.* (2017), for example. Hereafter, the measured data are used as a boundary condition in Eq. (4). This approach is only taken as part of the validation process of the measurements, but could potentially be used during the optimization to improve the high-frequency response of the driver. On the right-hand side of Fig. 9, the definition of the radial measurement line is shown with respect to the loudspeaker driver. In the same figure, the left-hand side shows the distribution of the measured axial velocity amplitudes at different frequencies as a function of the radial direction. It is seen that at the frequencies 500 Hz and 1 kHz, the diaphragm velocity is uniform and hence, the loudspeaker is operating as a piston. However, at 4 and 5.5 kHz, the velocity is no longer uniform along the radial direction. The same is seen in Fig. 10 where the measured magnitude and phase response of the loudspeaker are plotted between 1 and 8 kHz. Some variation in the axial velocity magnitude is already observed between 2 and 3 kHz and above 5–6 kHz, it is clear that the piston assumption is invalid. Hence, it is expected that the LPM will start to give inaccurate results in this range. This is also close to the upper limit in which the optimization is carried out. It should be noted that the model does not capture the effect of asymmetric breakup modes, which would require an entire model without the symmetry assumptions.

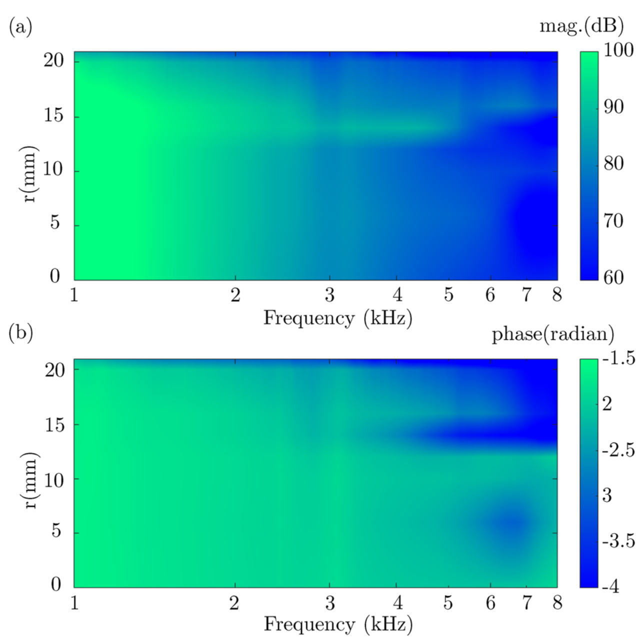

FIG. 10. (Color online) The data from the LDV velocity measurements of the loudspeaker driver as a function of the radius and frequency. (a) The magnitude of the velocity in decibels calculated using a reference of 1 nm/s, (b) the associated unwrapped phase in radians.

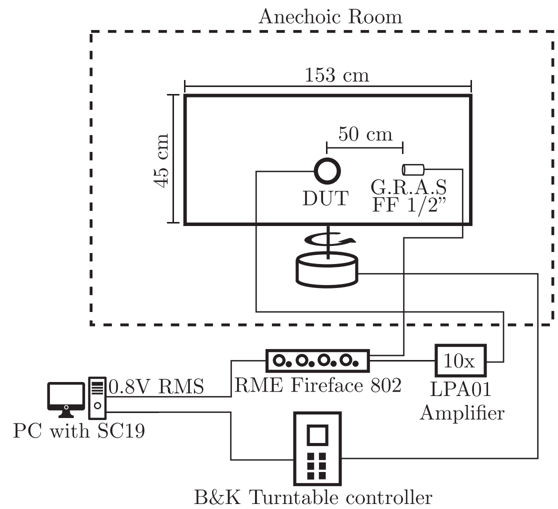

FIG. 11. The sequence performs a sweep from 100 Hz to 20 kHz with 0.8 V RMS. This signal is sent through a RME Fireface 802 (Haimhausen, Germany), which sends it to an amplifier, this signal is applied on the speaker terminals (DUT). After each sweep, the platform with the DUT is rotated 5°. The data acquisition is done with a ½ in. free-field microphone from G.R.A.S. (Holte, Denmark).

B. Measurements on a finite baffle

The SPL frequency response of the optimized loudspeaker system at different angles is measured on a finite rectangular baffle mounted on a turntable placed in an anechoic chamber. A schematic drawing of the entire measurement setup and the device under test (DUT) are shown in Fig. 11. Also, Fig. 12 shows the definition of the measurement angle which here is defined in the same way as ψ_j.

Figure 13 shows the angle dependent SPL frequency response measurements at the angles 35°, 45°, 55°, and 65°

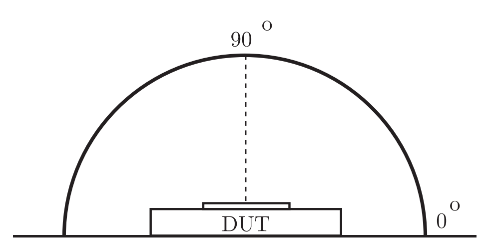

FIG. 12. In the graphs, 90° corresponds to the on-axis response, whereas 0° corresponds to being face-parallel with the table.

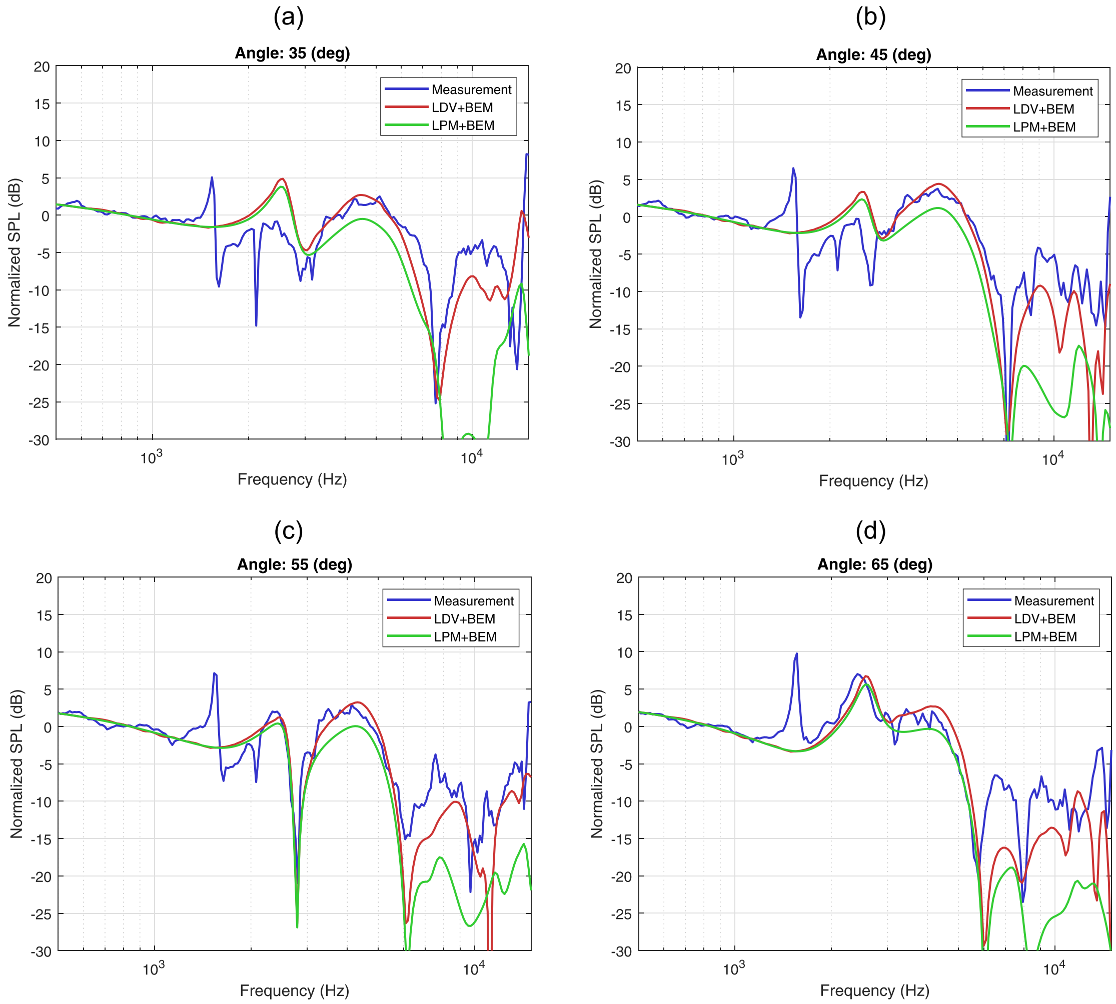

FIG. 13. (Color online) Comparison of the simulated and the measured SPL response at (a) 35°, (b) 45°, (c) 55°, (d) 65°. The blue curves are the measurements, the red curves are BEM simulations based on the LDV measurements, and the green curve is the BEM simulation model coupled to the LPM. The simulations are adapted to match the conditions of the measurements. However, the simulations still assume infinite baffle conditions. All the results are normalized to the average SPL between 700 Hz and 1 kHz.

(blue curves). The figure also includes the corresponding BEM simulations using both the LPM (green curve) and the LDV (red curve) description of the loudspeaker. Note that the measurement angles used in the experiment do not match precisely with the field points employed in the optimization process (Fig. 4). The main difference between simulations and the measurements is that the simulations assume an infinite baffle. Additionally, the BEM simulations do not include the lens support structures. It should be noted that the effect of the support structures has been tested in preliminary simulations showing that their effect on the frequency response is minimal within the optimization range. Overall, the tendencies of the simulated and the measured frequency responses are similar; however, with some discrepancies in the range from 1–3 kHz. In general, as expected, the LDV-based simulations seem to predict the SPL response behaviour better above 3 kHz as compared to the simulations based on the LPM. Albeit there is an overall good matching behaviour between the simulations and measurements, the responses also reveal discrepancies. Close to 1.5 kHz, all the measured data show large sudden variations in the SPL responses. We conjecture that the deviations from the simulations are associated with mechanical resonant vibrations of the lens structure (which is verified by the full FEM-based vibroacoustic study presented in Sec. VII C). As a result, close to the mechanical lens resonances, 5–10 dB difference between the measured data and the simulations are observed. Moreover, above 8 kHz, the LPM and LDV-based simulations fail to give very reliable results. Nevertheless, the LDV-based simulations give better response predictions as compared to using the LPM-based simulations at higher frequencies.

C. Full vibroacoustic simulation of the driver, cabinet, and lens assembly

To investigate and further explain the discrepancies observed between the acoustic BEM simulations and the measurements, this section presents a full FEM vibroacoustic study of the loudspeaker. The vibroacoustic simulations are carried out in the simulation software [COMSOL

https://doi.org/10.1121/10.0017859

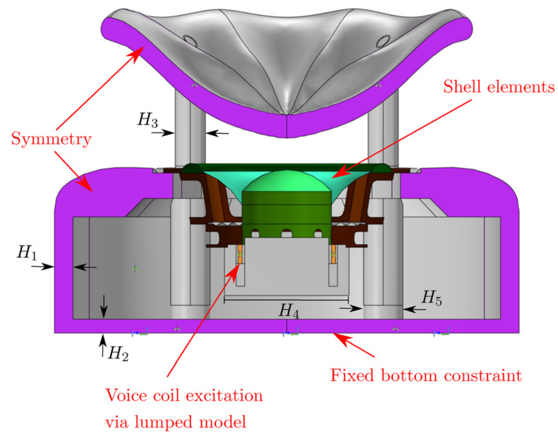

FIG. 14. (Color online) The geometry and boundary conditions of the vibroacoustic model. The sizing parameters are given by: $H_1 = 4$ mm, $H_2 = 3$ mm, $H_3 = 6.5$ mm, $H_4 = 2.68$ cm, and $H_5 = 8.5$ mm.

(Stockholm, Sweden) Multiphysics version 6.0]. In the FEM model, the structural parts of the loudspeaker unit (magnet, basket, spider, diaphragm, dust cap, and suspension) are modelled using shell elements, and the lens and cabinet assembly are modelled with solid structural elements. The geometry and boundary conditions are depicted in Fig. 14. The model is a pure FEM model where exterior radiation conditions are fulfilled using the perfectly matched layer (PML) boundary condition in COMSOL. Also, the model relies on half symmetry. The frequency dependent SPL response of the full vibroacoustic model and the measurements at the four measurement angles are shown in Fig. 16. As is observed in the figure, the full vibroacoustic FEM model is able to accurately capture the vibrations of the lens occurring due to a structural resonance and its impact on the acoustical response. Moreover, the vibration pattern near the lens resonance is shown in Fig. 15. From the figure, it is seen that the lens is in fact vibrating with a displacement magnitude similar to the loudspeaker diaphragm and hence

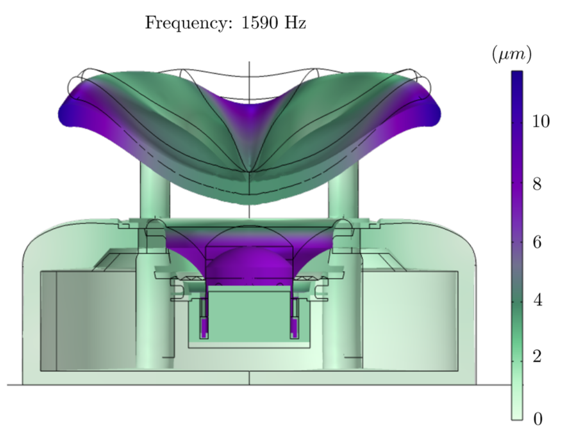

FIG. 15. (Color online) Forced vibrations of the loudspeaker system near the lens resonance calculated using a full vibroacoustic FEM simulation. The colormap corresponds to the displacement magnitude of the structural displacement in micrometers. The geometry is deformed according to the structural displacement with the solid black lines representing the geometry at rest. The geometric deformations are exaggerated for visualization purposes.

will contribute significantly to the exterior acoustic response. Hence, it might be desirable to include these effects into the optimization using a full vibroacoustic model. However, it can be challenging to limit the effect of vibrations merely using shape optimization. It is often only possible to alter the frequency at which the resonance is located (Andersen *et al.*, 2022b). Reducing the effect of the mechanical resonance will require either decoupling or damping of the vibrating structure. In addition to the discrepancies near the lens resonance, it is also observed that for the measurement angles 35° and 45°, Figs. 16(a) and 16(b), respectively, the simulations and measurements also deviate with several decibels in the region from 2–3 kHz. Nevertheless, these discrepancies are not observed to the same extent for the angles of 55° and 65°.

VIII. DISCUSSION

The measurement results have presented the feasibility of using acoustic shape optimization in a wideband multi-frequency optimization setting. However, several challenges persist. One of the drawbacks of shape optimization is the dependency on the initial design guess. In the presented optimization, it has been difficult to drastically change the off-axis performance. Hence, searching for better starting guesses will be required to further improve the performance. Also, the problem of colliding boundaries has been solved by restricting the design freedom through the linking of control points. However, more elaborate boundary overlap constraints could be used to improve the design space. Moreover, only the z-direction of the control points is used during the optimization process. Including $r_{i,j,k}$ and $\theta_{i,j,k}$ as design variables will significantly improve the design space and possible design choices. However, in that case, it is the authors' experience that it is challenging to maintain a reasonable quality of the underlying computational mesh. Therefore, a solution might be to use re-meshing when the mesh is too distorted or a constraint that ensures a sufficient quality of the mesh during optimization iterations. Alternatively, a more elaborate parameterization method, such as the level-set approach, could be used (Dilgen *et al.*, 2022). All the above suggested improvements come at an increased computational cost to an already very expensive optimization strategy. Hence, such improvements will be difficult to implement in the presented optimization framework. Several steps to improve the computational speed could be investigated by using, e.g., a model reduction method or distributed computing to evaluate the cost function at individual frequencies in parallel.

On one hand, the measured results show similar behaviour as the simulations in the optimization range. On the other hand, not unexpectedly, mechanical vibrations play a role in the measured results. To illustrate these discrepancies, the mechanical effects due to lens vibrations are shown in a full-vibroacoustic simulation. It would be desirable to include these effects in the shape optimization process. Nevertheless, this would drastically increase the

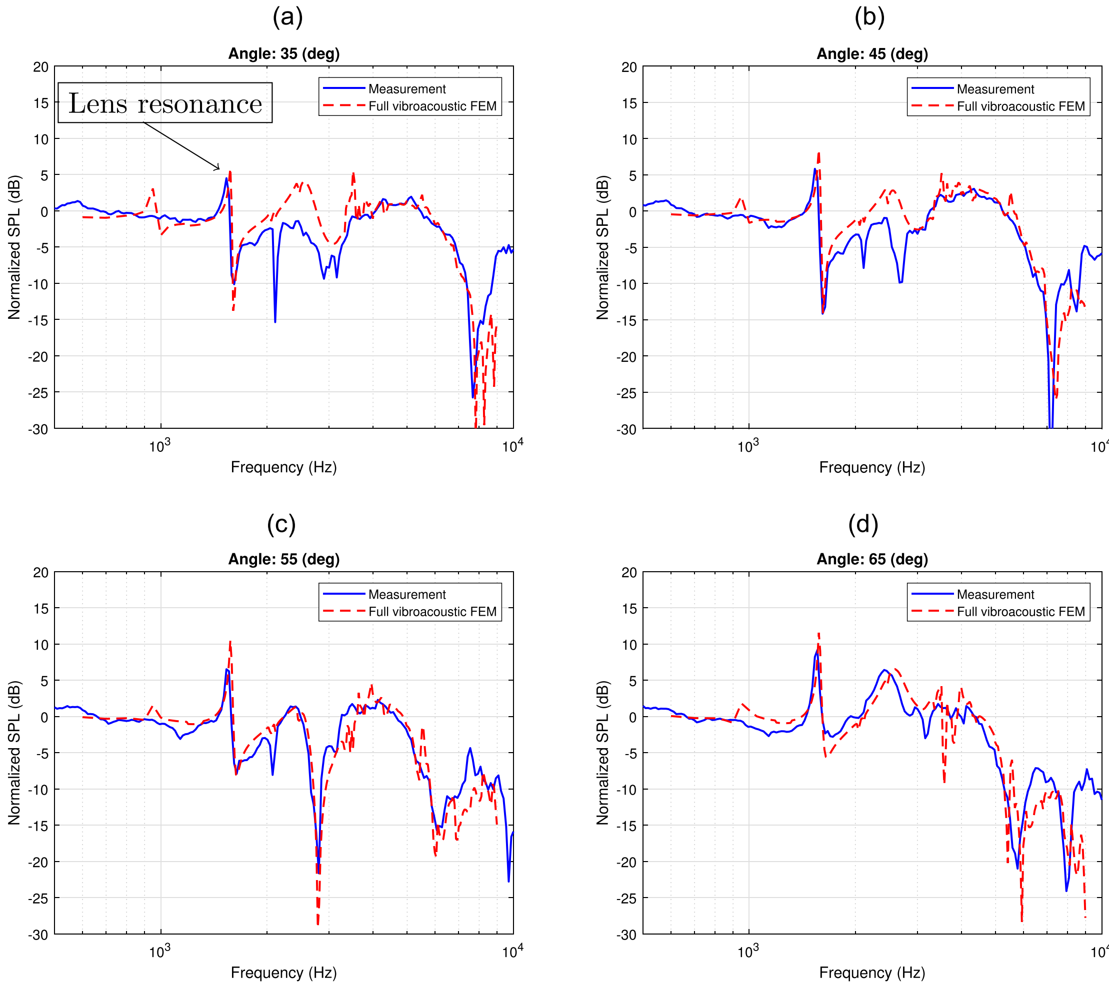

FIG. 16. (Color online) Comparison of the measured SPL frequency response and a full vibroacoustic model of the loudspeaker system. The figure includes measurements at the angles: (a) 35°, (b) 45°, (c) 55°, (d) 65°. The blue curves correspond to the measured data, and the red dashed curves are full vibroacoustic simulations using COMSOL Multiphysics. All the results are normalized to the average SPL between 700 Hz and 1 kHz.

computational complexity and is therefore considered future work when a more efficient solver setup is available. It is also noted that the discrepancies observed at 35° and 45° in the frequency range from 1–3 kHz are expected to be perceptually noticeable as they are in a frequency range where human hearing is particularly sensitive.

IX. CONCLUSION

In conclusion, the validity of an acoustic shape optimization procedure is experimentally confirmed and its application to loudspeaker design is shown. The result of the optimization shows that it is possible to minimize the cost function over a relatively broad frequency band. However, from a loudspeaker performance perspective, having the lens in an up-firing configuration creates peaks and notches in the frequency response that are not necessarily wanted. Improving this behaviour or removing these effects will require significantly different starting guesses. Also, the coupled BEM and LPM approach limits the upper frequency range of the optimization procedure. Therefore, if optimization at higher frequencies is to be performed, one can apply the LDV simulation approach during the optimization. Also, as shown, mechanical vibrational effects are very likely to play a role. Hence, one should consider including the full vibroacoustic model in the shape optimization framework.

ACKNOWLEDGMENT

The authors would like to thank Kuno Mønster for the help with the 3D printing of the loudspeaker cabinet and the lens. This work was supported by the industrial postdoc program, Innovation Fond Denmark, Grant No. 0154-00004B.

Andersen, P. R., Cutanda Henriquez, V., Aage, N., and Kook, J. (**2022a**). "3D shape optimization of loudspeaker cabinets for uniform directivity," Struct. Multidisc. Optim. **65**, 343.

Andersen, P. R., Cutanda Henriquez, V., Aage, N., Seongyeol, G., and Kook, J. (**2022b**). "Vibro-acoustic shape optimization for radiation problems: Application to compact loudspeakers," in *Proceedings from International Congress on Acoustics*, Gyeongju, Korea, A16, pp. 11–18.

Bai, M. R., Chen, R. L., and Wang, C. J. (**2009**). "Electroacoustic analysis of an electret loudspeaker using combined finite-element and lumped-parameter models," J. Acoust. Soc. Am. **125**(6), 3632–3640.

Bang, and Olufsen. (**2014**). "Bang and olufsen, beolab 20," https://www.bang-olufsen.com/da/dk/hoejttalere/beolab-20 (Last viewed July 14, 2022).

Bängtsson, E., Noreland, D., and Berggren, M. (**2003**). "Shape optimization of an acoustic horn," Comput. Methods Appl. Mech. Eng. **192**(11-12), 1533–1571.

Bezzola, A. (**2018**). "Numerical optimization strategies for acoustic elements in loudspeaker design," in *145th Audio Engineering Society International Convention, AES 2018*, pp. 1–12.

Chen, L. L., Lian, H., Liu, Z., Chen, H. B., Atroshchenko, E., and Bordas, S. P. (**2019**). "Structural shape optimization of three dimensional acoustic problems with isogeometric boundary element methods," Comput. Methods Appl. Mech. Eng. **355**, 926–951.

Christensen, R. (**2020**). "Shape and topology optimization of loudspeaker drivers," in *Proceedings from COMSOL Conference*, Grenoble/Online, pp. 1–7.

Christiansen, R. E., and Sigmund, O. (**2016**). "Designing meta material slabs exhibiting negative refraction using topology optimization," Struct. Multidisc. Optim. **54**(3), 469–482.

Collini, L., Farina, A., Garziera, R., Pinardi, D., and Riabova, K. (**2017**). "Application of laser vibrometer for the study of loudspeaker dynamics," Mater. Today: Proc. **4**(5), 5773–5778.

Creixell Mediante, E., Jensen, J. S., Naets, F., Brunskog, J., and Larsen, M. (**2018**). "Adaptive parametric model order reduction technique for optimization of vibro-acoustic models: Application to hearing aid design," J. Sound Vib. **424**, 208–223.

Dilgen, S. B., Aage, N., and Jensen, J. S. (**2022**). "Three dimensional vibroacoustic topology optimization of hearing instruments using cut elements," J. Sound Vib. **532**, 116984.

Dong, H. Y., Cheng, Q., Song, G. Y., Tang, W. X., Wang, J., and Cui, T. J. (**2017**). "Realization of broadband acoustic metamaterial lens with quasi-conformal mapping," Appl. Phys. Express **10**(8), 087202.

DTU Computing Center (**2022**). "DTU Computing Center resources," https://doi.org/10.48714/DTU.HPC.0001 (Last viewed April 11, 2023).

Gao, H., Fang, X., Gu, Z., Liu, T., Liang, S., Li, Y., and Zhu, J. (**2019**). "Conformally mapped multifunctional acoustic metamaterial lens for spectral sound guiding and Talbot effect," Research **2019**, 1748537.

Juhl, P. M., and Cutanda Henríquez, V. (**2010**). "Openbem - an open source boundary element method software in acoustics," in *Proceedings Internoise 2010*, Lisbon, Portugal, pp. 1–10.

Kinsler, L. E. (**2000**). *Fundamentals of Acoustics* (Wiley, Hoboken, NJ).

Leach, W. M. (**2010**). *Introduction to Electroacoustics & Audio Amplifier Design* (Kendall Hunt, Dubuque, IA).

Lee, G.-T., Kim, J.-B., and Son, S.-H. (**2015**). "Slit-firing sound plate design with slim elliptical speaker," in *Audio Engineering Society Convention 138*, http://www.aes.org/e-lib/browse.cfm?elib=17739, pp. 1–13 (Last viewed April 11, 2023).

Mellow, T., and Kärkkäinen, L. (**2022**). "On the scattering of a disk source by a rigid sphere for directivity broadening," J. Acoust. Soc. Am. **151**, 4114–4125.

Nielsen, D. G., Agerkvist, F. T., and Jensen, J. S. (**2021**). "Achieving a flat, wideband frequency response of a loudspeaker unit by numerical optimization with requirements on its directivity," J. Acoust. Soc. Am. **150**(2), 663–672.

Nielsen, D. G., Andersen, P. R., Jensen, J. S., and Agerkvist, F. T. (**2020**). "Estimation of optimal values for lumped elements in a finite element–lumped parameter model of a loudspeaker," J. Theor. Comp. Acout. **28**(2), 2050012.

Schmidt, S., Wadbro, E., and Berggren, M. (**2016**). "Large-scale three-dimensional acoustic horn optimization," SIAM J. Sci. Comput. **38**(6), B917–B940.

Sederberg, T., and Parry, S. R. (**1986**). "Free-form deformation of solid geometric models," SIGGRAPH Comput. Graph. **20**(4), 151–160.

Udawalpola, R., and Berggren, M. (**2008**). "Optimization of an acoustic horn with respect to efficiency and directivity," Int. J. Numer. Meth. Engng. **73**(11), 1571–1606.

Udawalpola, R., Wadbro, E., and Berggren, M. (**2011**). "Optimization of a variable mouth acoustic horn," Int. J. Numer. Meth. Engng. **85**(5), 591–606.

Van den Wyngaert, J. C. E., Schevenels, M., and Reynders, E. P. B. (**2021**). "Shape optimization of studs in double-leaf plasterboard walls for maximal broadband sound insulation and minimal material use," Appl. Acoust. **183**, 108307.